Evaluation of multipactor thresholds for coaxial lines subject to surface conditioning for the WEST ion cyclotron antenna

Eva Al Hajj Sleiman, Julien Hillairet, Mohamed Belhaj, Sarah Dadouch

Evaluation of Multipactor Thresholds for Coaxial Lines Subject to Surface Conditioning for the WEST Ion Cyclotron Antenna

Eva Al Hajj Sleiman[1, 2], Julien Hillairet[1], Mohamed Belhaj[2], and Sarah Dadouch[2]

[1]CEA, IRFM, 13108 Saint Paul Les Durance, France
[2]ONERA, DPHY, Université de Toulouse, 31055 Toulouse, France

***Abstract*— Multipactor voltage threshold charts and scaling laws for $30\,\Omega$ circular coaxial geometries, relevant to the WEST Ion Cyclotron Resonance Heating antennas, are reproduced using a developed multipactor decision-making algorithm relying on Spark-3D electron time-evolution data. The developed methodology is validated by comparing the simulated multipactor powers to the measured multipactor power thresholds, for a $50\,\Omega$ coaxial geometry. The effects of the conditioning, for a WEST antenna-relevant surface sample, on the total electron emission yield and surface properties are studied. The consequences of the conditioning phase on the multipactor voltage thresholds for coaxial transmission lines of $30\,\Omega$ and $50\,\Omega$ characteristic impedance are also highlighted. It is shown that preliminary baking and conditioning suppress or reduce the range in which multipactor can be triggered.**

I. Introduction

Multipactor is an electron multiplication mechanism occurring in RF devices, in a vacuum environment, when the electron mean free path is longer than the electrode separation distance [1]–[3]. Multipactor can be observed in many applications such as space applications [4], tokamak fusion reactors' RF components [5]: antennas, transmission lines, RF windows, and as well as, in particle accelerator structures [6] or microwave vacuum tubes [7].

Multipactor can have detrimental effects on devices' normal operation: increasing the system noise level leading to signal degradation [8], outgassing [9], raising the local temperature of the device that may damage internal components [10], loading the cavity with the build-up of an electron cloud [11], and generating undesirable harmonics [12]. If not stopped, the temperature rise, and the subsequent increase of pressure due to particles' desorption, caused by multipactor, can trigger a corona discharge which may lead to components' destruction [9], [13].

In nuclear fusion devices' radio-frequency heating and current drive systems, the consequences of multipactor-initiated discharges can be problematic, and limit the operation reliability or the maximum coupled power [14], [15]. In addition, this effect can increase the reflected power to the source, which can damage the high RF power sources (klystrons or tetrodes). RF components, such as vacuum feed-through (also called windows), can be damaged by excess heat production or metallization of the ceramics produced by arc-induced sputtering [16].

High power Ion Cyclotron (IC) RF antennas are used on the fusion experimental tokamak WEST (Cadarache, France) [17]. These antennas use coaxial lines made of stainless steel covered with a $50\,\mu\mathrm{m}$ silver coating, and are of $30\,\Omega$ characteristic impedance. Silver has been selected as coating material to reduce RF losses. Before being operated, these antennas are subject to in-situ conditioning treatments: baking and RF conditioning. RF conditioning, is an antenna-surface conditioning technique based on short (ms) RF power pulses, and is used to clean and remove the impurities deposited on the surfaces. The effects of these treatments on the multipactor thresholds are addressed herein.

As multipactor experiments are expensive to realize, especially with complex components of large dimensions such as the ones used as heating systems for fusion reactors, developing numerical tools for multipactor prediction is valuable. However, the multipactor thresholds are highly dependent on the RF device geometry and material properties [18], but also the solver configurations. Hence, particular attention must be paid to carry out realistic multipactor analysis.

The purpose of this paper is twofold. In the first part, we describe the methodology to reliably determine the RF power thresholds, for which multipactor can be triggered inside any coaxial sections. This is done using a developed multipactor prediction algorithm that relies on the temporal evolution of the electron population evaluated by the software product Spark-3D [19][1] for a given RF power and frequency. In a circular coaxial line, multipactor may be developed for zones between a lower and an upper voltage or power thresholds [1], [11]. At the difference of most recent references studies [18], [20], [21], we are specifically interested in the highest multipactor threshold, which affects high power RF applications for fusion reactors. To validate our calculation methodology, we have compared the simulated power multipactor thresholds to measured data from [22]. In addition, we have reproduced the scaling laws for coaxial geometries reported in references [1], [11], [23], where the predicted multipactor thresholds are compared qualitatively with the experimental results from [1], to verify the proposed scaling laws.

In the second part, the total electron emission yield (TEEY), for the coating material constituting the IC antennas used on

[1]Version 1.6.3.

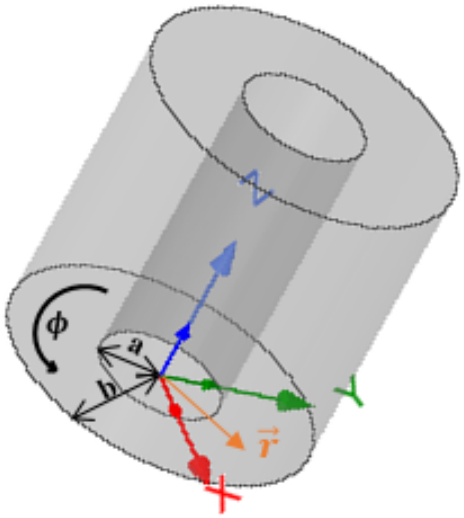

Fig. 1. Representation of the vacuum space of a cylindrical coaxial cable.

WEST, is measured in various relevant operational conditions such as baking and temperature, and the surface properties are studied in terms of the desorbed species during conditioning. In addition, the impact of the surface conditioning of this material on the multipactor thresholds for coaxial transmission lines of characteristic impedance $30\,\Omega$ and $50\,\Omega$ is explored.

II. Multipactor Prediction of Coaxial Geometries

A. Multipactor Conditions

Total electron emission yield (TEEY), generally referred to as σ, is defined as the mean number of back-scattered and secondary electrons emitted per incident primary electron. It is a function of the impact energy, and the angle of incidence of primary electrons [24], [25]. For a given angle of incidence, the TEEY curve is generally identified by: the maximum TEEY (σ_{max}) corresponding to the peak impact energy (E_{max}); and the minimum and maximum incident energies where $\sigma = 1$, defined as the first (E_{c1}) and second (E_{c2}) crossover energies.

For multipactor to occur, two conditions must be satisfied [1], [2]: *i)* one necessary but not sufficient condition, that the impact energy of electrons colliding with an electrode must be sufficient, *i.e.*, it should exceed the first cross-over energy of the material, so that the total electron emission yield (TEEY) of the electrode surface is greater than one, for secondary electrons to be released. *ii)* the second condition is the resonance condition for the electron's motion to be synchronized with phase change of the RF electric field [1], [25]. As the multipactor thresholds are very sensitive to the electron emission yield, the knowledge of the material TEEY is essential for accurate multipactor predictions [18].

B. Geometry Model and Previous Findings

Consider a uniform circular coaxial transmission line consisting of an inner conductor of radius a and an outer conductor of radius b. $d = b - a$, is the gap distance between electrodes. The characteristic impedance Z_0 of the coaxial transmission line is given by [26]

$$Z_0 = \frac{1}{2\pi}\sqrt{\frac{\mu}{\varepsilon}}\ln\frac{b}{a} \tag{1}$$

where ε and μ are respectively the permittivity and the permeability of the filling material between the inner and outer conductor, which is the vacuum in our study case ($\varepsilon = \varepsilon_0$, $\mu = \mu_0$; ε_0, and μ_0 being respectively the vacuum permittivity and the vacuum permeability).

For a coaxial cable, two different types of multipactor can occur [7], [11]: double-sided multipactor, an electron multiplication occurring between the inner and outer conductor, and single-sided multipactor where electrons both come from and impinge on the outer conductor. Moreover, in coaxial geometries, there is a minimum multipactor voltage threshold beyond which multipactor is triggered in the vacuum space between the conductors, and a maximum multipactor voltage threshold after which no multipactor takes place [11].

In a coaxial line structure, the electric field is inhomogeneous and inversely proportional to the radial distance from the centre of the inner conductor, if the TEM mode is dominant. In this geometry, a ponderomotive force, also known as the Miller force [7], tends to push the electrons toward the outer region of lower electric field amplitude, causing, once the conditions are met, a single-sided multipactor on the outer conductor. In most cases, this force also leads to a shorter transit time, when travelling from the inner conductor to the outer conductor, than that when going from the outer to the inner conductor. For resonance to occur, the sum of the two-way transit times should be equal to an integer number of RF cycles [11].

The time-harmonic electric field, in the vacuum between the electrodes of a circular coaxial line, is radial and is given by [24], [25]

$$\mathbf{E}(r,t) = \frac{V}{r\ln(b/a)}\sin(\omega t)\,\vec{\mathbf{r}} \tag{2}$$

where $\vec{\mathbf{r}}$ is the radial unit vector (Fig. 1) and V is the peak voltage magnitude, defined as the integral of the electric field along the radial direction, *i.e.* $V(t) = \int_a^b E(r,t)\,dr$. For a matched line, the RF power flowing into the line is given by $P = V^2/(2Z_0)$.

Many authors have investigated the multipactor threshold voltage V_{mp} of such geometry using analytical, numerical and experimental work for which main findings are recalled here. Vaughan studied, in [2], the simplest case of multipactor for two parallel plates separated by a distance d and driven by an RF voltage at frequency f. He also found that, the lower and the upper multipactor voltages, bounding the region where multipactor can occur within the geometry, are proportional to $(fd)^2$.

In [27], Woo stated that the similarity principle leads to two scaling relations for the coaxial cables. In the first one, for various products $f \times d$, the multipactor breakdown voltages are proportional to $(fd)^2$, in agreement with Vaughan's analytical studies [2], but provided that there is no change in the multipactor mode. Moreover, he revealed that the upper

multipactor voltage thresholds follow remarkably well this law for all b/a. For the lower multipactor voltage thresholds, he found that the $(fd)^2$ is only true for a high b/a ratio, and the exponent is less than 2 otherwise, where the breakdown voltage is more sensitive to surface conditions. In the second law, for constant product $f \times d$, two coaxial cables of different dimensions but with the same characteristic impedance, *i.e.*, ratio b/a, exhibit the same breakdown voltages.

In his paper, Woo validated experimentally the scaling relations applied to coaxial transmission lines. A shift to higher values, for breakdown voltages of the multipactor region, has been observed with increased characteristic impedance or equivalently the ration b/a. He explained this by the decrease of multipactor's probability of occurrence because of the increased gradient of the electric field for increasing b/a.

In [11], the authors derived an approximate solution (position and velocity formulas) for the non-linear differential equations of electron motion in coaxial transmission lines. They found that, a single-sided multipactor, for which the time between collisions corresponds to an integer number of RF periods, exhibits a $(fb)^2 Z_0$ voltage dependence. This result is in agreement with numerical calculations done by Somersalo [23] and Pérez [28].

Udiljak et al. [11] also proved that when the inner radius is of the order of the outer one, that is for low characteristic impedance, the multipactor analysis for the coaxial is similar to that of a parallel plate geometry and double-sided multipactor is dominant. But, in the case when the inner radius is smaller than a determined threshold equal to 58% of the outer radius, that is for high characteristic impedance, a high-order double-sided multipactor is no more possible and only a single-sided multipactor is present, provided that the initial velocity is low and fast oscillating motions of the electron's position are small.

For a double-sided multipactor, they derived a multipactor voltage scaling law given by $(fd)^2$. This law is valid for the first order resonance, for all values of the characteristic impedance, whereas for higher order resonances, it is valid only for low characteristic impedance [11]. In agreement with the results found by Woo [27], their analysis showed that, an increase in the characteristic impedance of the line leads to an increase in the multipactor threshold, and to a narrower region for the first order multipactor.

However, the range of validity of their work is restrained to GHz range of frequencies. Where the taken assumption that $\Lambda \ll (\omega R)^2$, where $\Lambda = eE_o b/m$, E_o being the electric field on the outer conductor, e and m respectively the charge and mass of one electron, and R the time-averaged position of the electron, is valid for GHz frequencies [24]. Hence, in the MHz range of frequencies used in this work, this analytical method could not be applied, and an alternative should be found.

Somersalo, in [23], [29], developed a computational method to analyze the multipactor phenomenon in different RF structures to determine the multipactor power, type (single-sided or double-sided), and order. Somersalo analyzed the multipactor in a coaxial transmission line and extracted from the results four scaling laws: *i)* the single-sided multipactor voltage, for a coaxial cable of fixed characteristic impedance, follows $(fd)^2/(n+1)$, n being the multipactor order, *ii)* a scaling law for the double-sided multipactor voltage, with respect to the frequency and dimensions, that agrees with Woo's experimental laws $(fd)^2$, and *iii)* for varying line impedance, the single-sided, and double-sided multipactor voltages follow respectively $(fd)^2 Z_0$ and $(fd)^2 Z_0^{3/2}$.

In [20], the authors simulated the minimum voltage thresholds, for the onset of multipactor, using the commercial software CST Particle Studio and compared the results with Woo's published experiments [27]. They concluded that the level of agreement is dependent on the model of the secondary emission electron yield data.

Most of these studies focused on predicting the minimum breakdown voltage for multipactor onset. However, for magnetic confinement-based fusion reactors' applications where high power (MW range) antennas are used, we are also interested in predicting the maximal breakdown voltage triggering the multipactor phenomenon, for which little literature exists.

C. TEEY measured data

We are interested in studying the multipactor thresholds, for coaxial transmission lines of characteristic impedance $30\,\Omega$ and $50\,\Omega$, using different TEEY measurements data curves for WEST antennas' representative samples, made of stainless steel and coated with $10\,\mu\mathrm{m}$ Ni and $50\,\mu\mathrm{m}$ Ag, *i.e.*, more than 2 times the skin depth at the lowest frequency considered in this work.

For the results discussed in Section IV-B, the TEEY curve corresponds to the measurements performed at the ONERA laboratory, at normal incidence at $53\,^{\circ}\mathrm{C}$, using an ultrahigh vacuum facility dedicated to electron emission characterization [30], for a silver-coated stainless-steel sample baked at $190\,^{\circ}\mathrm{C}$ for two hours before the measurements. These measured values of TEEY, for the silver-coated sample, are illustrated in Fig. 2. The first crossover energy for this TEEY curve, is $E_{c1} \approx 27\,\mathrm{eV}$ (first incident energy where $\sigma = 1$). This parameter is known to affect multipactor thresholds [18].

For the results discussed in Section IV-C, the TEEY data curves are measured, at normal incidence, for a silver-coated stainless steel sample, subjected to the representative operational conditions for the WEST antennas in terms of baking, conditioning, and operational temperature, which are described below.

Like several fusion reactors and particle accelerators, the tokamak WEST relies on preliminary baking and RF conditioning phases, before operating, to improve the machine vacuum and cleanliness conditions. These commissioning phases lead to modify the electron emission properties of the surfaces constituting the device. The bake-out under vacuum and the RF conditioning, are two methods known to reduce the TEEY of the surfaces [31]. In this study, the RF conditioning is simulated by an in-situ electron bombardment. This conditioning treatment of the samples, also known as the dose effect, is a surface treatment method based on impacting the surfaces with an electron beam of specific intensity, for a given time [6]. In particular, for the treatments to be representative of the WEST-tokamak case, the sample was first baked at

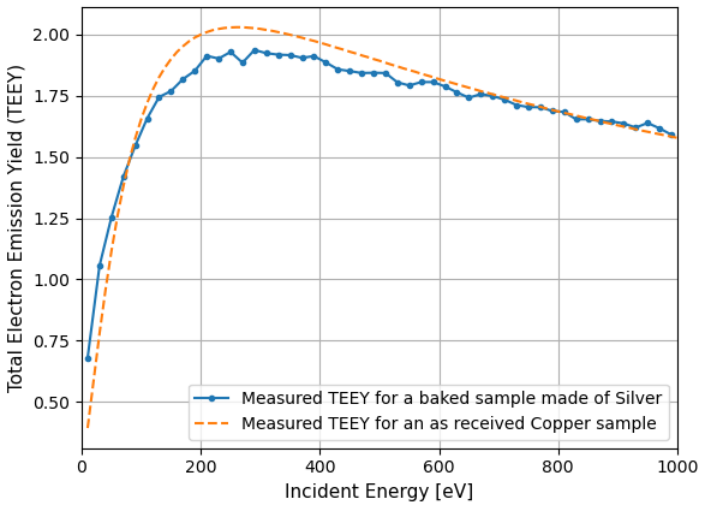

Fig. 2. In blue, the measured TEEY data, at normal incidence, for a stainless-steel sample coated with silver and baked at 190 °C for two hours. In orange, the measured TEEY data, at normal incidence, for an as-received copper sample.

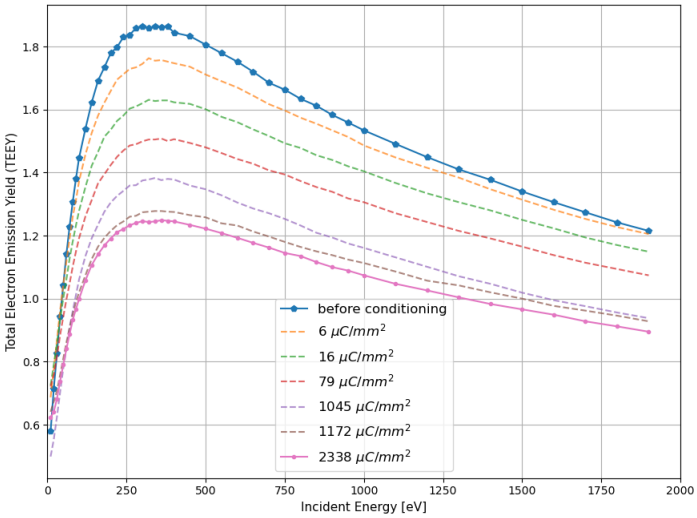

Fig. 3. TEEY measurements for a baked silver-coated stainless steel sample, maintained at 70 °C, before conditioning, and after impacting its surface by the following cumulative electron doses (from top to bottom): $6\,\mu\mathrm{C\,mm^{-2}}$, $16\,\mu\mathrm{C\,mm^{-2}}$, $79\,\mu\mathrm{C\,mm^{-2}}$, $1045\,\mu\mathrm{C\,mm^{-2}}$, $1172\,\mu\mathrm{C\,mm^{-2}}$, and $2338\,\mu\mathrm{C\,mm^{-2}}$.

200 °C for three days and then maintained at a temperature of 70 °C during TEEY measurements. This sample was then, subject to different cumulative electron doses, to simulate the RF conditioning effect, and after each dose, the TEEY was measured in situ. These TEEY measurements are represented in Fig. 3. These measurements clearly show the effect of the baking and the conditioning with dose, on the TEEY properties, where the maximum TEEY is reduced, and the first crossover energy becomes greater than the case of the TEEY measurements before conditioning.

The values of the maximum TEEY and the first crossover energy, for these TEEY curves, corresponding to the different electron doses, are given in Table I. These values show the saturation of the TEEY measurements properties, in terms of the first crossover energy and the maximum TEEY, when the sample is subject to an electron dose greater than $1172\,\mu\mathrm{C\,mm^{-2}}$; because when the dose is increased from $1172\,\mu\mathrm{C\,mm^{-2}}$ to $2338\,\mu\mathrm{C\,mm^{-2}}$ (almost doubled), the first crossover and the maximum TEEY change only slightly (with a relative difference of $\sim 2\,\%$ for the maximum TEEY, and $\sim 6\,\%$ for the first crossover energy). Therefore, once the surface state reaches the TEEY properties given in the curve corresponding to the electron dose of $2338\,\mu\mathrm{C\,mm^{-2}}$, the conditioning effects become negligible. In addition, the surface won't be severely re-contaminated, because this treatment is done in-situ under vacuum, and the surface is not re-exposed to air.

The contaminants desorption was evidenced by monitoring the chemical surface modifications of the sample, after each conditioning phase, using an X-ray Photoelectron Spectroscopy (XPS) [32]. XPS, is a surface-sensitive technique, used to identify the chemical state of the elements present on the last few nanometers of the sample surface. The XPS spectra, acquired in-situ, at the conditioning phases, show the presence of contaminants and in particular, carbon and oxygen as well as silver. The atomic concentration of these different elements, for the different electron doses, are represented in Figure 4. For the first three electron doses $6\,\mu\mathrm{C\,mm^{-2}}$, $16\,\mu\mathrm{C\,mm^{-2}}$, and $79\,\mu\mathrm{C\,mm^{-2}}$ a decrease in the concentration of both oxygen and carbon is noticed, indicating hence the desorption of the contaminants from the sample surface. Above the third electron dose, a re-increase in the concentration of carbon is observed, leading to an eventual decrease in silver atomic concentration. This phenomenon has been observed before [33], [34], and is attributed to the electron gun used for conditioning, which becomes a source of contamination due to evacuated molecular fragments containing the carbon element. Therefore, conditioning phases are important to eliminate the hydrocarbon elements and adsorbed oxides on the surface of the IC antennas and lead to the reduction of the TEEY. Nevertheless, if the conditioning time exceeds $(D_s \times S)\,/I$, no effect on the surface properties will be noticed (where D_s is the electron dose above which no variation in the TEEY properties is observed, S is the conditioned antenna surface, and I being the conditioning current). The effect of these surface treatments on multipactor thresholds, for coaxial transmission lines of characteristic impedance $30\,\Omega$ and $50\,\Omega$, is addressed in the next section.

TABLE I
TEEY PARAMETERS FOR THE SEVEN CURVES OF FIG. 3.

Cumulative Dose [$\mu\mathrm{C\,mm^{-2}}$]	$TEEY_{max}$	E_{c1} [eV]
0 (before conditioning)	1.86	46
6	1.76	45
16	1.63	50
79	1.51	60
1045	1.38	88
1172	1.28	94
2338	1.25	100

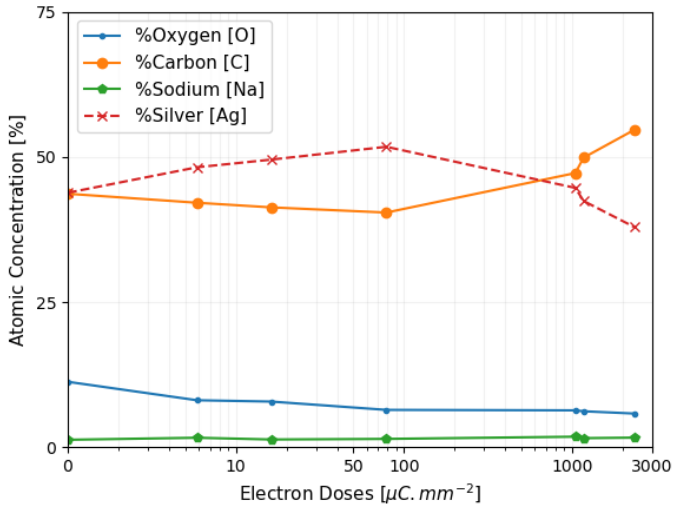

Fig. 4. Surface atomic concentration for the different elements, found on the surface of the baked silver-coated stainless steel sample, at each conditioning phase.

III. Multipactor Thresholds Modelling

A. Multipactor Threshold Definition

Spark-3D has its own implemented automatic multipactor power threshold determination algorithm. Nevertheless, it only determines the lower threshold for which multipactor occurs. Since in this study we are also looking for upper thresholds, we have implemented an algorithm to predict both multipactor thresholds, based on the growth rate of the electron population. The algorithm is generic and relies only on the data of the time-evolution electron numbers, given by any software solving the electron dynamics' equations inside the geometry. Using these data, a coefficient a is calculated to predict an increase or decrease of the electron population

$$a = \frac{N_{e,f} - N_e}{t_f - t} \tag{3}$$

where $N_{e,f}$, N_e are respectively, the number of electrons at the end of the simulation, and at a pre-selected time $t < t_f$. In that way, the growth rate or decrease of electron population over the last N periods, where N is a predefined number dependent on the geometry, determines whether or not the multipactor is triggered inside the geometry: if $a > 0$, multipactor is assumed; otherwise there is no multipactor. In addition, an algorithm to scan powers is used, along with the implemented thresholds-prediction algorithm, in order to determine accurately the lower and upper multipactor thresholds for a given coaxial geometry. The developed algorithm agrees with the implemented Spark-3D algorithm, predicting the lower multipactor bounds as depicted in Figure 5.

B. Software Details

To use Spark-3D, the cartography of the electromagnetic fields of any geometry must be imported before running the multipactor calculation. To this end, ANSYS-HFSS is used for solving the electromagnetic fields of the geometries in the frequency domain.

TABLE II
Comparison between the measured multipactor power thresholds and the simulated power thresholds for a $50\,\Omega$ coaxial transmission made of copper.

Freq [MHz]	Lower multipactor power [W]		Upper multipactor power [W]	
	Measurements	Simulations	Measurements	Simulations
100	64	55	180	161
120	74	73	414	383
140	119	117	619	681

For a given geometry to be analyzed, TEEY boundary conditions obtained from the measurements described in the previous section, are applied to all the metallic surfaces of the analyzed geometry.

The initial number of seeded electrons is a user-defined value, and these electrons are seeded once at the beginning of the simulation run. By default in Spark-3D, the initial positions of seeded electrons are weighted to favour regions of the high electric field. A convergence study on the multipactor thresholds against the number of initial electrons is systematically made, for each different geometry.

The electron emitted energy distribution, used in Spark-3D, is a Maxwell-Boltzmann distribution [35] with most probable energy of $4\,\mathrm{eV}$. The elastic and inelastic back-scattered electrons are taken into consideration, and the angular distribution for secondary electrons is taken into account using a cosine law.

For each power scanned, the software will generate a file representing the temporal evolution of the number of electrons for that power, using an electron tracker algorithm that is based on a leap-frog method [36]. Then, using the multipactor decision algorithm, based on the rate of growth of electrons, the lower and upper power multipactor bounds are determined. It should be noted that Spark-3D does not take the space charge effect into account.

IV. Results

A. Comparison with experimental data

To validate the methodology and the developed algorithms, a comparison between the multipactor experimental data, given in [22], and the simulation results is done. The measured power multipactor at frequency $100\,\mathrm{MHz}$, $120\,\mathrm{MHz}$, and $140\,\mathrm{MHz}$ are obtained for a coaxial transmission line of characteristic impedance $50\,\Omega$, and separation distance $d \approx 1.1$ cm. This coaxial was made of copper and its measured TEEY data curve is represented in Figure 2 (curve in orange). Both the measured and simulated multipactor powers are given in Table II, and show that the difference between the simulation results obtained by averaging the multipactor predicted thresholds from 10 runs, and the measured thresholds did not exceed $15\,\%$, validating hence the methodology and the developed algorithms.

B. Scaling laws' validation for a $50\,\Omega$ silver-coated coaxial line

For the simulations discussed here, the measured TEEY tabulated data for silver-coated material, illustrated in blue in

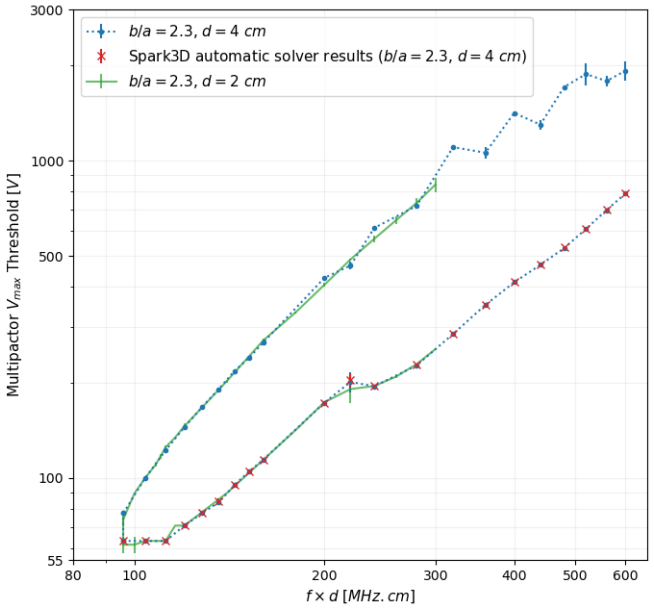

Fig. 5. Simulated susceptibility data for a coaxial transmission line of characteristic impedance $Z_0 = 50\ \Omega$, and inter-electrode distance $d = 4$ cm (blue) and $d = 2$ cm (green), while varying the frequency in the range $[10 - 150]$ MHz. The plots are obtained for the TEEY curve of the silver-coated material in Fig. 2 (blue curve), using the prediction algorithm based on the rate of growth applied to the time-particle evolution results of Spark-3D. The results obtained by the automatic solver of Spark-3D are plotted in red.

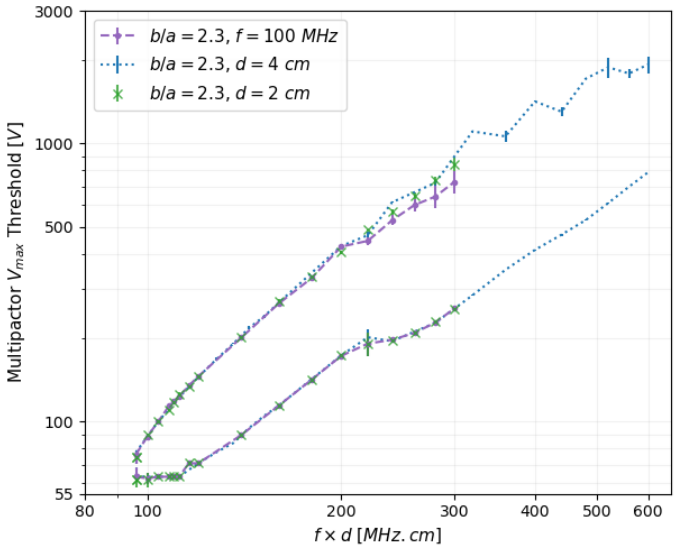

Fig. 6. In blue and green, the simulated susceptibility data were obtained by varying the frequency, and fixing the separation distance d. The curve in purple, corresponds to the simulated susceptibility data when the separation distance d is varied in the range $[0.4 - 3]$ cm, and the frequency is fixed to 100 MHz. Plots are obtained for the TEEY curve, of the silver-coated sample (Fig. 2), for a coaxial transmission line of characteristic impedance $Z_0 = 50\ \Omega$, and applying the developed algorithm for multipactor prediction.

Fig. 2, are imported into Spark-3D. In all the simulations, the vacuum region is initially seeded with 2000 electrons and the developed algorithm relying on the electrons' growth rate is applied. It should also be noted that there is no DC magnetic field applied during multipactor simulations. There is no reflection in the coaxial transmission line (matched situation). The thresholds are given in voltage rather than in power, as further studies will focus on unmatched configurations for which voltage is more meaningful than power.

In Fig. 5, the frequency is varied between 10 MHz and 150 MHz for a 50 Ω coaxial transmission line of two different separation distances. The green curve corresponds to the average voltage multipactor thresholds and error bars, for a coaxial transmission line of separation distance $d = 2$ cm. Whereas, the blue dotted curve corresponds to the average multipactor threshold voltages and the error bars for a coaxial transmission having a separation distance d of 4 cm. For both curves, the average multipactor voltages are calculated from 10 consecutive runs, using our developed multipactor prediction algorithm. In red, the average lower multipactor voltage thresholds, obtained by the automatic solver of Spark-3D, and corresponding to the blue curve case, are represented. These results show a very good agreement between the predicted thresholds using our implemented algorithm, and the lower predicted thresholds obtained by the automatic solver of Spark-3D. The maximum multipactor voltages are plotted as a function of the $f \times d$ product, for the measured TEEY values of the silver sample (represented in blue in Figure 2). It can be remarked that the standard deviation of the numerical errors, for the 10 simulation runs, are very small in logarithmic scale representation.

The results' shape is similar to the one obtained by Woo [1], [27]. Nevertheless, the multipactor thresholds obtained by simulation are not quantitatively comparable to the measured thresholds given in [1], [27], because the measurements were done for a copper coaxial, of undetermined TEEY, whereas simulations were done for a silver-coated coaxial. Only the global shape of the multipactor thresholds in function of the $f \times d$ product is to be compared. Using the prediction algorithm based on the electrons' growth rate, it can be remarked that the results have the same shape as Woo's experimental results and confirm the dependence stated by Woo and further authors: for the upper multipactor voltage thresholds the dependence is $(fd)^2$, whereas for the lower multipactor voltage thresholds the dependence is found to be proportional to $(fd)^p$, where p is a fitting parameter, ranging between 1 and 2, and determined for each multipactor mode. Moreover, the simulation results validate that, for a fixed characteristic impedance, two coaxial cables of different dimensions exhibit the same multipactor thresholds at a fixed $f \times d$ product.

Inside the region bordered by the multipactor threshold points, multipactor is triggered for this geometry, whereas outside of it no multipactor can take place.

According to the second scaling law proposed by Woo [27], for a coaxial transmission line of fixed characteristic impedance, the multipactor thresholds should be the same for a given $f \times d$, independently of the choice of the frequency and the inter-electrode distance. To prove that this is indeed the case for the simulated multipactor thresholds independently of the scanned parameter (f or d), the maximum multipactor voltage thresholds obtained for a 50 Ω coaxial transmission line of variable separation distance d and operating at a

fixed frequency of 100 MHz, are represented in purple in the Figure 6 (the blue and green data points of Figure 5 are re-plotted here for comparison purpose). The results show that, in the $f \times d$ product range $[20 - 600]$ MHz $\cdot$ cm, the multipactor voltage thresholds for the $50\,\Omega$ coaxial of fixed distance d and variable frequency are in strong correspondence with the multipactor voltage thresholds obtained for a $50\,\Omega$ coaxial of variable distance and fixed frequency.

C. WEST operational conditions' effect on Multipactor thresholds

On the tokamak WEST, the coaxial lines are of characteristic impedance $Z_0 \approx 30\ \Omega$, where $b = 230/2$ mm and $a = 140/2$ mm. For this reason, in this section, we investigate the effect of the WEST-relevant conditioning phase, on the multipactor thresholds for coaxial transmission lines of characteristic impedance $50\,\Omega$, and $30\,\Omega$. To study the operational conditioning effects, simulations were carried out using two TEEY measurements' curves of Fig. 3: before impacting the surface with an electron beam (before conditioning), and after impacting it with a cumulative electron dose of $2338\,\mu\mathrm{C\,mm^{-2}}$.

In Fig. 7, the average simulated multipactor voltage thresholds and the error bars, calculated from 3 consecutive runs, for a matched coaxial transmission line of characteristic impedance $50\,\Omega$ and a separation distance d of 4 cm, are plotted in violet. The average simulated multipactor voltage thresholds and the error bars, for a coaxial transmission line of characteristic impedance $30\,\Omega$ and a separation distance d of 4.5 cm, are plotted in grey. The maximum multipactor voltages are plotted as a function of the $f \times d$ product, for the TEEY curves corresponding to the non-conditioned and the fully conditioned measurements, represented in Fig. 3. The frequency is scanned in the range $[20 - 150]$ MHz. It is found that the conditioning both increases the lower multipactor thresholds and decreases the upper multipactor thresholds. This results in decreasing the overall region area in which the multipactor is expected to be triggered in the coaxial transmission line. Moreover, the conditioning suppresses the multipactor occurrence at low $f \times d$ products, as shown in Fig. 7. These effects could be explained by the increase in the first crossover energy, and the decrease in the maximum TEEY values, as illustrated in Table I. Owing to the IC high voltage operational conditions, the multipactor region should be bypassed by achieving an RF rise time less than the multipactor rise time. This large jump in the RF voltage, is known as multipactor push-through, as the multipactor is not sustained in the antenna since there is no sufficient time for it to be developed. Therefore, reducing the multipactor region has an effect on the reduction of the efforts needed to achieve the push-through.

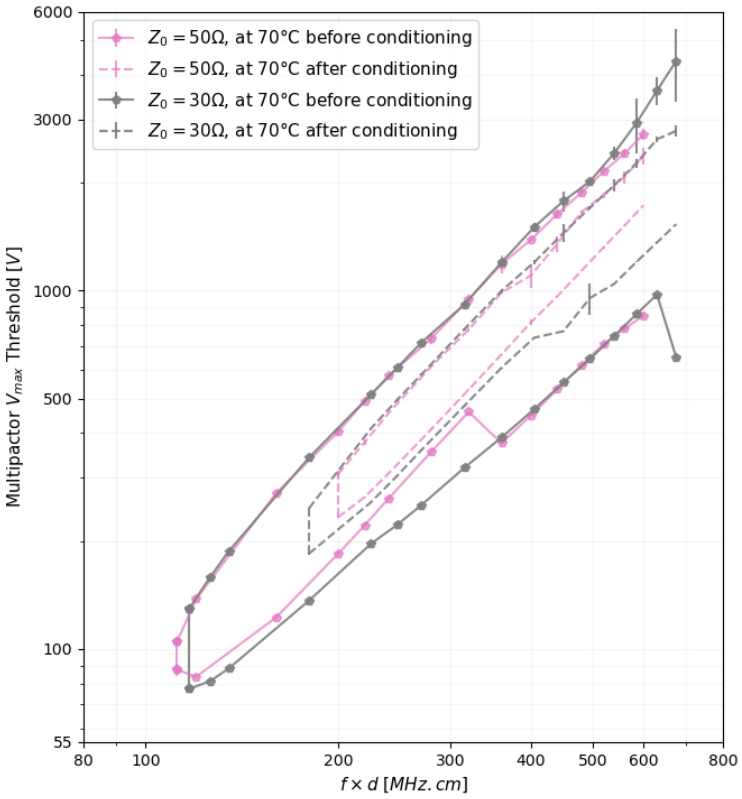

Fig. 7. The violet (respectively gray) plots are the simulated susceptibility voltage multipactor data for a coaxial transmission line of characteristic impedance $Z_0 = 50\ \Omega$ ($Z_0 = 30\ \Omega$), and inter-electrode distance $d = 4$ cm ($d = 4.5$ cm), while varying the frequency in the range $[10 - 150]$ MHz. Plots are obtained for the first and the last TEEY curves represented in Fig. 3, corresponding to the non-conditioned case, and the case after impacting the sample with a cumulative electron dose of $2338\,\mu\mathrm{C\,mm^{-2}}$ (fully conditioned).

V. Conclusion

A multipactor detection algorithm is proposed to determine the minimum and maximum voltages limiting the range of voltages where multipactor is triggered in any coaxial transmission line. We compared this methodology to multipactor measured experimental results, obtained for a $50\,\Omega$ coaxial line made of copper, and we validated the scaling laws proposed for this type of geometries. The TEEY properties' variations, resulting from the operational conditions of WEST, are studied. Moreover, the dependence of the multipactor thresholds on the TEEY curve properties, in particular, the maximum TEEY and the first cross-over energy, is highlighted in this paper using two different TEEY curves for the same material: one measured TEEY curve before conditioning the sample, and a measured experimental data points after fully-conditioning the surface with a cumulative electron dose of $2338\,\mu\mathrm{C\,mm^{-2}}$. It is shown that both baking and dose effect conditioning, reduce the $f \times d$ product range over which the multipactor is triggered inside the geometry, and reduce the multipactor voltages' range for each $f \times d$ product.

VI. Acknowledgment

This work is co-financed by CEA-Cadarache, and ONERA-Toulouse. We would like to thank Yolanda Gomez Martinez, and all the team at LPSC - Grenoble for providing the TEEY copper sample measurements. This work has been carried out within the framework of the EUROfusion Consortium, funded by the European Union via the Euratom Research and Training Programme (Grant Agreement No 101052200

– EUROfusion). Views and opinions expressed are however those of the author(s) only and do not necessarily reflect those of the European Union or the European Commission. Neither the European Union nor the European Commission can be held responsible for them.

REFERENCES

[1] R. Woo, "Final report on RF Voltage Breakdown in Coaxial Transmission Lines," report 32-1500, National Aeronautics and Space Administration, October 1970.

[2] J. Vaughan, "Multipactor," *IEEE Transactions on Electron Devices*, vol. 35, pp. 1172–1180, July 1988.

[3] R. A. Kishek, Y. Y. Lau, L. K. Ang, A. Valfells, and R. M. Gilgenbach, "Multipactor discharge on metals and dielectrics: Historical review and recent theories," *Physics of Plasmas*, vol. 5, pp. 2120–2126, May 1998.

[4] J. De Lara, F. Perez, M. Alfonseca, L. Galan, I. Montero, E. Roman, and D. Garcia-Baquero, "Multipactor prediction for on-board spacecraft RF equipment with the MEST software tool," *IEEE Transactions on Plasma Science*, vol. 34, pp. 476–484, April 2006.

[5] J. Hillairet, M. Goniche, N. Fil, M. Belhaj, and J. Puech, "Multipactor in High Power Radio-Frequency Systems for Nuclear Fusion," in *MULCOPIM (Multipactor, Corona and Passive Intermodulation)*, April 2017.

[6] V. Petit, M. Taborelli, H. Neupert, P. Chiggiato, and M. Belhaj, "Role of the different chemical components in the conditioning process of air exposed copper surfaces," *Physical Review Accelerators and Beams*, vol. 22, p. 083101, August 2019.

[7] S. Apostolos, *Modeling of Long-Term Multipactor Evolution in Microwave Components Including Dielectric Layers*. PhD thesis, École Polytechnique Fédérale de Lausanne, 2015.

[8] V. E. Semenov, E. I. Rakova, N. A. Zharova, J. Rasch, D. Anderson, and J. Puech, "Simple model of the rf noise generated by multipacting electrons," *Journal of Physics D: Applied Physics*, vol. 47, p. 055206, February 2014.

[9] E. Sorolla, *Contribution to Modeling Multipactor and Corona Discharges in High Power Electromagnetic Fields*. PhD thesis, EPFL, 2012.

[10] L.-K. Ang, Y. Lau, R. Kishek, and R. Gilgenbach, "Power deposited on a dielectric by multipactor," *IEEE Transactions on Plasma Science*, vol. 26, pp. 290–295, June 1998.

[11] R. Udiljak, D. Anderson, M. Lisak, V. E. Semenov, and J. Puech, "Multipactor in a coaxial transmission line. I. Analytical study," *Physics of Plasmas*, vol. 14, p. 033508, March 2007.

[12] R. Udiljak, D. Anderson, P. Ingvarson, U. Jordan, U. Jostell, L. Lapierre, G. Li, M. Lisak, J. Puech, and J. Sombrin, "New method for detection of multipaction," *IEEE Transactions on Plasma Science*, vol. 31, no. 3, 2003.

[13] F. Höhn, W. Jacob, R. Beckmann, and R. Wilhelm, "The transition of a multipactor to a low-pressure gas discharge," *Physics of Plasmas*, vol. 4, pp. 940–944, April 1997.

[14] T. P. Graves, S. J. Wukitch, B. LaBombard, and I. H. Hutchinson, "Effect of multipactor discharge on Alcator C-Mod ion cyclotron range of frequency heating," *Journal of Vacuum Science & Technology A: Vacuum, Surfaces, and Films*, vol. 24, pp. 512–516, May 2006.

[15] M. Goniche, C. El Mhari, M. Francisquez, S. Anza, J. Belo, P. Hertout, and J. Hillairet, "Modelling of power limit in RF antenna waveguides operated in the lower hybrid range of frequency," *Nuclear Fusion*, vol. 54, p. 013003, January 2014.

[16] H. Kim, J. Verboncoeur, and Y. Lau, "Modeling rf window breakdown: from vacuum multipactor to rf plasma," *IEEE Transactions on Dielectrics and Electrical Insulation*, vol. 14, 08 2007.

[17] J. Bucalossi, J. Achard, O. Agullo, T. Alarcon, L. Allegretti, H. Ancher, G. Antar, S. Antusch, V. Anzallo, C. Arnas, D. Arranger, J. F. Artaud, M. H. Aumeunier, S. G. Baek, X. Bai, J. Balbin, C. Balorin, T. Barbui, A. Barbuti, J. Barlerin, V. Basiuk, T. Batal, O. Baulaigue, A. Bec, M. Bécoulet, E. Benoit, E. Benard, J. M. Benard, N. Bertelli, E. Bertrand, P. Beyer, J. Bielecki, P. Bienvenu, R. Bisson, V. Bobkov, G. Bodner, C. Bottereau, C. Bouchand, F. Bouquey, C. Bourdelle, J. Bourg, S. Brezinsek, F. Brochard, C. Brun, V. Bruno, H. Bufferand, A. Bureau, S. Burles, Y. Camenen, B. Cantone, E. Caprin, S. Carpentier, G. Caulier, N. Chanet, O. Chellai, Y. Chen, M. Chernyshova, P. Chmielewski, W. Choe, A. Chomiczewska, G. Ciraolo, F. Clairet, J. Coenen, L. Colas, G. Colledani, J. Colnel, P. Coquillat, E. Corbel, Y. Corre, S. Costea, X. Courtois, T. Czarski, R. Daniel, J. Daumas, M. D. Combarieu, G. D. Temmerman, P. D. Vries, C. Dechelle, F. Deguara, R. Dejarnac, J. M. Delaplanche, L. F. Delgado-Aparicio, E. Delmas, L. Delpech, C. Desgranges, P. Devynck, S. D. Genova, R. Diab, A. Diallo, M. Diez, G. Dif-Pradalier, M. Dimitrova, B. Ding, T. Dittmar, L. Doceul, M. Domenes, D. Douai, H. Dougnac, X. Duan, L. Dubus, N. Dumas, R. Dumont, F. Durand, A. Durif, A. Durocher, F. Durodié, A. Ekedahl, D. Elbeze, S. Ertmer, A. Escarguel, F. Escourbiac, K. Ezato, F. Faisse, N. Faure, N. Fedorczak, P. Fejoz, C. Fenzi-Bonizec, F. Ferlay, M. Firdaouss, L. Fleury, D. Flouquet, A. Gallo, Y. Gao, X. Garbet, J. Garcia, J. L. Gardarein, L. Gargiulo, P. Garibaldi, S. Garitta, J. Gaspar, E. Gauthier, P. Gavila, S. Gazzotti, F. Gely, M. Geynet, S. Gharafi, P. Ghendrih, I. Giacalone, C. Gil, S. Ginoux, S. Girard, E. Giroux, G. Giruzzi, C. Goletto, M. Goniche, T. Gray, E. Grelier, H. Greuner, E. Grigore, C. Grisolia, A. Grosjean, A. Grosman, D. Guibert, D. Guilhem, C. Guillemaut, B. Guillermin, R. Guirlet, J. P. Gunn, Y. Gunsu, T. Gyergyek, A. Hakola, J. Harris, J. C. Hatchressian, W. Helou, P. Hennequin, C. Hernandez, K. Hill, J. Hillairet, T. Hirai, G. T. Hoang, M. Houry, T. Hutter, F. Imbeaux, N. Imbert, I. Ivanova-Stanik, R. Jalageas, A. Jardin, L. Jaubert, G. Jiolat, A. Jonas, P. Joubert, A. Kirschner, C. Klepper, M. Komm, M. Koubiti, J. Kovacic, M. Kozeiha, K. Krieger, K. Krol, B. Lacroix, L. Laguardia, V. Lamaison, H. Laqua, C. Lau, Y. Lausenaz, R. Lé, M. L. Bohec, N. Lefevre, N. Lemoine, E. Lerche, M. Lewerentz, Y. Li, M. Li, A. Liang, P. Linczuk, C. Linsmeier, M. Lipa, X. Litaudon, X. Liu, J. Llorens, T. Loarer, A. Loarte, T. Loewenhoff, G. Lombard, J. Lore, P. Lorenzetto, P. Lotte, M. Lozano, B. Lu, R. Lunsford, G. Luo, P. Magaud, P. Maget, J. F. Mahieu, P. Maini, P. Malard, K. Malinowski, P. Manas, L. Manenc, Y. Marandet, J. L. Marechal, S. Marek, C. Martin, E. Martin, A. Martinez, P. Martino, D. Mazon, P. Messina, L. Meunier, D. Midou, Y. Mineo, M. Missilian, R. Mitteau, B. Mitu, P. Mollard, V. Moncada, T. Mondiere, J. Morales, M. Moreau, P. Moreau, Y. Moudden, G. Moureau, D. Mouyon, M. Muraglia, A. Nagy, T. Nakano, E. Nardon, A. Neff, F. Nespoli, J. Nichols, S. Nicollet, R. Nouailletas, M. Ono, V. Ostuni, C. Parish, H. Park, H. Parrat, J. Y. Pascal, B. Pégourié, F. P. Pellissier, Y. Peneliau, M. Peret, Y. Peysson, E. Pignoly, G. Pintsuk, R. Pitts, C. Pocheau, C. Portafaix, M. Poulos, P. Prochet, A. P. Sitjes, M. Rasinski, G. Raup, X. Regal-Mezin, C. Reux, B. Riccardi, J. Rice, M. Richou, F. Rigollet, H. Roche, J. Romazanov, C. Ruset, R. Sabot, A. Saille, R. Sakamoto, T. Salmon, F. Samaille, A. Santagiustina, B. Santraine, Y. Sarazin, E. Serre, H. Shin, S. Shiraiwai, J. Signoret, J. Signoret, A. Simonin, O. S. Fettachi, Y. Song, A. Spring, P. Spuig, S. Sridhar, B. Stratton, C. Talatizi, P. Tamain, R. Tatali, M. Ténа, A. Torre, L. Toulouse, J. M. Travère, W. Treutterer, E. Tsitrone, E. Unterberg, G. Urbanczyk, D. V. Eester, G. V. Rooij, S. Vartanian, J. M. Verger, L. Vermare, D. Vézinet, N. Vignal, B. Vincent, S. Vives, D. Volpe, G. Wallace, E. Wang, L. Wang, Y. Wang, Y. Wang, T. Wauters, B. Wirth, M. Wirtz, A. Wojenski, J. Wright, M. Xu, Q. Yang, H. Yang, B. Zago, Zagorski, B. Zhang, X. Zhang, and X. Zou, "Operating a full tungsten actively cooled tokamak: overview of WEST first phase of operation," *Nuclear Fusion*, vol. 62, p. 042007, Feb. 2022. Publisher: IOP Publishing.

[18] N. Fil, M. Belhaj, J. Hillairet, and J. Puech, "Multipactor threshold sensitivity to total electron emission yield in small gap waveguide structure and TEEY models accuracy," *Physics of Plasmas*, vol. 23, p. 123118, December 2016.

[19] C. Vicente, "Multipactor and corona discharge: Theoretical fundamentals and analysis with CST and SPARK3D software tools," in *2017 IEEE International Symposium on Electromagnetic Compatibility & Signal/Power Integrity (EMCSI)*, (Washington, DC, USA), pp. 1–48, IEEE, August 2017.

[20] S. V. Langelloti, N. M. Jordan, Y. Y. Lau, and R. M. Gilgenbach, "CST particle studio simulations of coaxial multipactor and comparison with experiments," *IEEE Transactions on Plasma Science*, vol. 48, pp. 1942–1949, June 2020.

[21] A. Plaçais, J. Hillairet, M. Belhaj, and J. Puech, "A numerical and theoretical study of the multipactor appearance in the presence of a dc parallel electric field," *AIP Advances*, vol. 12, p. 025022, February 2022.

[22] Y. G. Martinez, J. Angot, M. Baylac, T. Cabanel, D. P. O., N. Emeriaud, and O. Zimmermann, "First measurements on multipactor study," in *Proceedings of the 12th International Particle Accelerator Conference*, vol. IPAC2021, (Campinas, SP, Brazil), JACoW Publishing, Geneva, Switzerland, 2021.

[23] E. Somersalo, P. Yla-Oijala, and D. Proch, "Analysis of multipacting in coaxial lines," in *Proceedings Particle Accelerator Conference*, vol. 3, pp. 1500–1502, May 1995.

[24] G. Becerra, *Studies of Coaxial Multipactor in the Presence of a Magnetic Field*. PhD thesis, Massachusetts Institute of Technology, June 2007.

[25] T. P. Graves, *Experimental Investigation of Electron Multipactor Dis-*

charges at Very High Frequency. PhD thesis, Massachusetts Institute of Technology, June 2006.

[26] P. A. Rizzi, *Microwave Engineering*. Upper Saddle River, New Jersey 07458: Prentice-Hall, 1988.

[27] R. Woo, "Multipacting discharges between coaxial electrodes," *Journal of Applied Physics*, vol. 39, pp. 1528–1533, February 1968.

[28] A. M. Perez, C. Tienda, C. Vicente, S. Anza, J. Gil, B. Gimeno, V. E. Boria, and D. Raboso, "Prediction of multipactor breakdown thresholds in coaxial transmission lines for traveling, standing, and mixed waves," *IEEE Transactions on Plasma Science*, vol. 37, October 2009.

[29] E. Somersalo, P. Yla-Oijala, D. Proch, and J. Sarvas, "Computational methods for analyzing electron multipacting in rf structures," *Particle Accelerators*, vol. 59, pp. 107–141, January 1998.

[30] M. Belhaj and S. Dadouch, "A simple method for energy calibration of kev incident electron beam using a contactless electrostatic voltmeter probe.," *Review of scientific instruments*, vol. 92, p. 083301, July 2021.

[31] V. Baglin, J. Bojko, C. Scheuerlein, O. Gröbner, T. M. Taborelli, B. Henrist, and N. Hilleret, "The secondary electron yield of technical materials and its variation with surface treatments," in *Seventh European Particle Accelerator Conference*, (Vienna, Austria), June 2000.

[32] S. Hofman, *Auger- and X-ray Photoelectron Spectroscopy in Materials Science*. Heidelberg: Springer Series in Surface Science, 2013.

[33] C. Scheuerlein and M. Taborelli, "Electron stimulated carbon adsorption in ultrahigh vacuum monitored by auger electron spectroscopy," *Journal Of Vacuum Science & Technology, A-Vacuum Surfaces and Films*, vol. 20, no. 1, 2002.

[34] R. Larciprete, D. R. Grosso, M. Commisso, R. Flammini, and R. Cimino, "Secondary electron yield of cu technical surfaces: Dependence on electron irradiation," *PHYSICAL REVIEW ACCELERATORS AND BEAMS*, vol. 16, 2013.

[35] E. Rudberg, "Inelastic scattering of electrons from solids," *Physical Review*, vol. 50, pp. 139 – 150, July 1936.

[36] C. Birdsall and A. Langdon, *Plasma Physics via Computer Simulations*. Boca Raton: CRC Press, 1991.